Journal of Materials Chemistry C

Accepted Manuscript

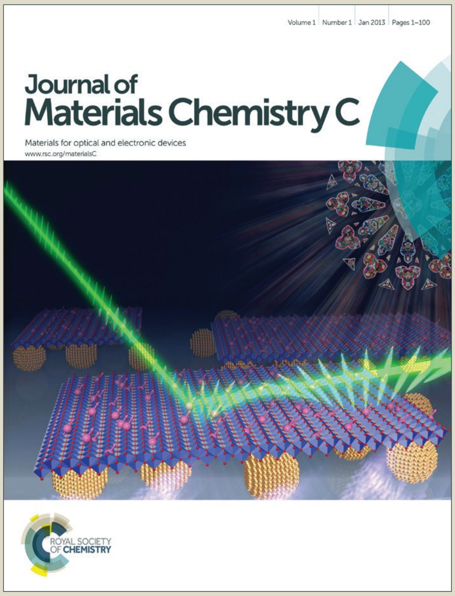

ROYAL SOCIETY OF CHEMISTRY

www.rsc.org/materialsC

Microfluidic Synthesis of Ultra-small Magnetic Nanohybrids for Enhanced Magnetic Resonance Imaging

Junmei Wang[1$], Kai Zhao[2$], Xiaomiao Shen[1$], Weiwei Zhang[1], Shaoxia Ji[1], Yujun Song[1]*, Xiaodong Zhang[2], Rong Rong[2], Xiaoying Wang[2]*

[1] Department of Physics, Center for Modern Physics, Engineering Center for Weak Magnetic Detection Beijing, School of Mathematics and Physics, University of Science & Technology Beijing, Beijing 100083, China; [2] Department of Radiology, Peiking University First Hospital, Beijing 100034, China

* Corresponding authors: Y.S., songyj@ustb.edu.cn; X.W., cjr.wangxiaoying@vip.163.com.

[$] Contribute to this article equally.

Abstract:

We have developed a core alloying and shell gradient doping strategy for the controlled surface modification of nanoparticles, realized by a coupled competitive reducing-nucleation and precipitation reaction controlled in microfluidic channels. Here it is extended in surface modification Fe and CoFe nanoparticles by doping zinc oxide and aluminum oxide to form well-dispersed stable ultra-small $Fe_{(1-x)}Zn_x@Zn_{(1-y)}Fe_yO\text{-}(OH)_z$ and $(CoFe)_{(1-x)}Al_x@Al_{(1-y)}(CoFe)_yO\text{-}(OH)_z$ nanohybrids as contrast agents for magnetic resonance imaging (MRI). They exhibit greatly enhanced T_1 weighted spin echo imaging and T_2 weighted spin echo imaging effects. Particularly, $(CoFe)_{(1-x)}Al_x@Al_{(1-y)}(CoFe)_yO\text{-}(OH)_z$ nanohybrids give a T_1 relaxation rate (R_1) of 0.156 (μg-CoFe/mL)$^{-1}$·s^{-1} and a T_2 relaxation rate (R_2) of 0.486 (μg-CoFe/mL)$^{-1}$·s^{-1}, much higher than the commercial gadopentetate dimeglumine (R_1 = 0.022 (μg-Gd/mL)$^{-1}$·s^{-1}; R_2 = 0.025 (μg-Gd/mL)$^{-1}$·s^{-1}). The R_1 of $(CoFe)_{(1-x)}Al_x@Al_{(1-y)}(CoFe)_yO\text{-}(OH)_z$ nanohybrids is also higher than superparamagnetic iron oxide (SPIO) nanoparticles (R_1 = 0.121 (μg-Fe/mL)$^{-1}$·s^{-1}). SPIO nanoparticles still show an excellent negative MRI contrast agent by the highest R_2 (5.07 (μg-Fe/mL)$^{-1}$·s^{-1}) and R_2/R_1 ratio (42) among these reagents.

Keywords: Nanohybrid, Microfluidic, Magnetic property, Surface modification, Magnetic resonance imaging

1. Introduction

With materials size decrease, surface and interface become more and more prominent for their properties, particularly in nanoscale materials and devices in which the quantum effect is more significant than that in bulk materials or single atoms.[1-15] Composition and structure controlled hybridization at nanoscale has become an effective approach for realizing multi-function, stability and/or embarking novel physicochemical properties of nanomaterials due to the surface and interface enhanced properties and the synergistic effect among components.[4,5,7-10,13,16-30] This innovative approach not only provides varieties of hybrid nanostructures for better understanding the surface enhancement and interface-coupling effects, but also offers a route for overcoming undesired conflicts between structures and performances that accompany size reduction, and even breaking down the quantum mechanical rule at nanoscale.[4,7,9,12,23,31-38] With the advancement of science and technology promoted by nanohybrids, controlled surface and interface modification of nanoparticles (NPs) has also become more and more urgent to fulfill their academic and industrial perspectives.[8,29,34,39-48] Synthesis of these hybrid NPs based on surface and interface modification requires a precise control over microstructures of each component and overcoming lattice mismatch or incompatibility among components.[4,18,20,29,36,49] [15]Controlled successive coating on preformed cores is an effective and versatile method, but still challenging, particularly for ultra-small nanohybrids with feature sizes less than 5 nm due to their large curvatures.[15,29,49,50]

Microfluidic approaches have achieved lots of success in the NPs synthesis due to their reduced scaling up risk and the precise control of thermodynamic and kinetic parameters in desired reaction stages along the microchannel[29,40,51]. Since the first synthesis of CdS by microfluidics in 2002[52], great progresses have been obtained in the morphology and structure control of NPs at large scale and sketching the formation mechanism of nanoparticles spatiotemporally. [4,23,40-43,46,51,53-56] We developed a general strategy for nanohybrids synthesis via coupled competitive reactions controlled by a hybrid microfluidic and batch-cooling process.[9,29,57] Owing to their abilities in spatiotemporally splitting the formation stages of NPs, nanohybrids of well-defined microstructures can be realized, as evidenced by the synthesis of varieties of magnetic NPs and metal-metal oxide NPs with unique magnetic or optical properties.[9,23,29,57] Herein, we extend this strategy in the surface/interface engineering of ultra-small magnetic nanoparticles for enhanced magnetic resonance imaging (MRI). Well-dispersed ultra-small magnetic-alloys@metal-oxides (i.e., $Fe_{(1-x)}Zn_x@Zn_{(1-y)}Fe_yO\text{-}(OH)_z$ and $(CoFe)_{(1-x)}Al_x@Al_{(1-y)}(CoFe)_yO\text{-}(OH)_z$) nanohybrids are synthesized. They exhibit integrated T_1 weighted spin echo imaging (T_1WI) and T_2 weighted spin echo imaging (T_2WI) effects at much lower dosages by comparing with the commercial Gd-based reagents. In addition, the $(CoFe)_{(1-x)}Al_x@Al_{(1-y)}(CoFe)_yO\text{-}(OH)_z$ nanohybrids show superior T_1WI effects than Fe_3O_4 NPs. Reasons that they preserve excellent mode-integrated MRI effects are analyzed according to their unique magnetic properties and surface/interface features.

2. Experiment Section

2.1 Assembly of the mixed microfluidic and batch-cooling process (hybrid process).

The hybrid process was designed and assembled by connecting preheating stainless steel tubing coils, a transparent polymer tubing (e.g., Teflon) a Y connector (e.g. PEEK), the thermostatic tank 1 and 2 and the cooling tank 3 for product receivers, as shown in Fig. s1 of the supporting information (SI).[29,34,57] This setup entails: one syringe pump for the metal-salt solution (e.g., $FeCl_2$ and/or $CoCl_2$ in N-methyl-2-pyrrolidone (NMP) or H_2O mixed with polyvinylpyrrolidone (PVP)) (1); one syringe pump for the reducing-agent solution (e.g., $NaBH_4$ in NMP) (2); two preheating stainless steel spirals (3-4) immersed in the thermostatic tank 1 (inner diameter (ID) = 127 μm, length (L) = 15 cm) for the heating of the metal-salt solution and the reducing-agent solution from 20 ^{o}C to 200^{o}C; one Y-mixer (ID = 250μm or more, L = 4~5mm) for the reactants to react to form precursors and then to initiate nucleation (5); one microtubing spiral (ID = 127~500μm, L = 25~50 cm) in the thermostatic tank 2 with temperature from 20°C to 200°C for finishing nucleation and growth of nanoparticles (6); and one product receiver (7) protected by inert gas (i.e., N_2), with temperature controlled from -15°C to 10°C by chilling or heating thermostatic tank 3.

2.2 Sequenced in-situ reduction of metal ions and precipitation of metal oxides for hybrid nanoparticle synthesis.

To realize multi-functionalization and/or robust surface protection in single NPs, alloyed core-shell NPs or nanohybrids with core alloying and shell gradient-doping are expected to work.[4,25,26,43] To this aim, a new synthesis strategy, or *in-situ* reduction of mixed-metal ions and precipitation of second-metal oxides by forming oxide-doping alloys as cores and oxide alloys as shells or surface-coating, was developed by directly introducing the second-metal salts with low standard electrode potential (i.e., Zn^{2+}: $V_0 = -0.763V$; Al^{3+}: $V_0 = -1.662V$) into the primary-metal-salt solutions (i.e., $FeCl_2$ or mixed $FeCl_2$ and $CoCl_2$). The following is the brief mechanism to form gradient core-shell structures using Fe-Zn based nanoparticles as example (Reaction 1-4 and Scheme 1) according to our previous study.[9,29,56]

$$Fe^{2+} + Zn^{2+} + BH_4^- + H_2O \rightarrow [Fe_{(1-x)}Zn_x]_{colloid}\cdot PVP + BO_2^- + H_2 \quad (1)$$

$$Zn^{2+} + 2BH_4^- + 2H_2O \rightarrow Zn(OH)_2 + 2BH_3 + 2H_2 \quad (2)$$

$$Fe^{2+} + 2BH_4^- + 2H_2O \rightarrow Fe(OH)_2 + 2BH_3 + 2H_2 \quad (3)$$

$$[Fe_{(1-x)}Zn_x]_{colloid}\cdot PVP + Zn(OH)_2 + Fe(OH)_2 \rightarrow [Fe_{(1-x)}Zn_x]@[Zn_{(1-y)}Fe_yO\text{-}(OH)_z]\cdot PVP + H_2O \quad (4)$$

According to their standard electrode potential, the primary-metal salts will be reduced together with some second-metal salts (Reaction 1) to form Fe and Zn atoms and/or Fe-Zn atom clusters, which is faster than the precipitation of the metal ions into metal hydroxides (Reaction 2 and 3), leading to the pre-formation of the second metal (Zn) doping Fe tiny nanocrystallites as initial cores after a transient nucleation (Step 1 in Scheme 1). Some of the surface atoms may be oxidized again to form very thin surface metal oxides. These second-metal ions and some of the primary-metal ions can play roles as precursors of shells or surface coatings on these preformed nanocrystallites (i.e., Zn alloyed Fe NPs) by producing hydroxide species via precipitation in the basic medium (Reaction 2 and 3, Step 2 in Scheme 1). Then the surface coatings grow thicker and thicker by co-absorbing the metal hydroxides and some of the metal atoms/clusters through the reducing (Reaction 1) and precipitation (Reaction 2 and 3) of the metal ions (Step 3 in Scheme 1). As the surface coatings grow up, some of the atoms will diffuse through the coatings into the cores and some of metal hydroxides will diffuse through the coating into the surfaces. Simultaneously, these molecules and atoms can self-arrange into different doping crystal structures during diffusion to form gradient structures (Step 4 in Scheme 1). These hydroxide species can be further changed into oxides by dehydration, as oxide shells or surface coatings in the coming drying process (Reaction 4). Consequently, hybrid magnetic-alloys@metal oxides (i.e., $Fe_{(1-x)}Zn_x@Zn_{(1-y)}Fe_yO\text{-}(OH)_z$) with the primary metal doped $ZnO\text{-}(OH)_z$ as surface coatings can be obtained. In addition, as they are re-dispersed into aqueous solution, hybrid gradient nanoparticles with more hydroxide groups can be formed. The detailed synthesis mechanism is described in our recent publication.[29]

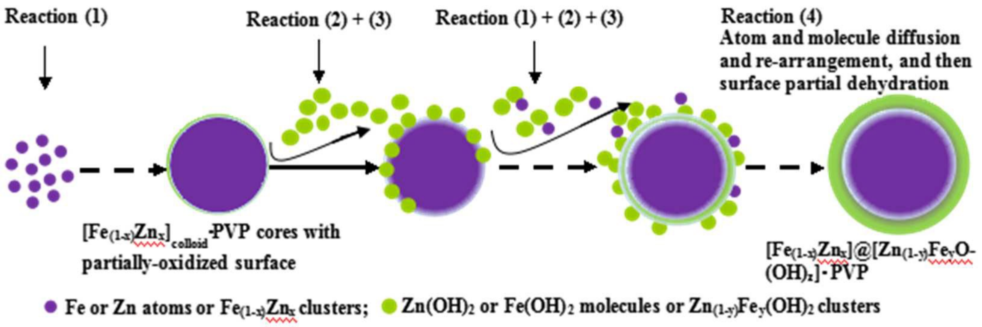

Scheme 1 Cartooned formation process of gradient core-shell nanostructures by coupled competitive reducing-precipitation reaction.

Synthesis of $Fe_{(1-x)}Zn_x@Zn_{(1-y)}Fe_yO\text{-}(OH)_z$ nanohybrids. Briefly, PVP of 0.5 g (Mw = 10000), $ZnCl_2$ of 0.097 g (0.71 mmol) and $FeCl_2{\cdot}4H_2O$ of 0.370 g (1.86 mmol) were dissolved into 50mL NMP to form the metal-salt solution. $NaBH_4$ of 0.373 g (9.8 mmol) was dissolved into 50 mL NMP to form the reducing solution. Then, the microfluidic synthesis was performed at 110°C under inert atmosphere (nitrogen) protection using the following procedure: 20 mL of metal-salt solution and 20 mL of reducing solution were sucked into each of the syringes and fixed in the platform of the syringe pump, which was introduced into the Y mixer (5) to fullfill the nucleation by the syringe pump at a flow rate of 1.5 mL/min per pump, and then the solution enters into the microchannel (6) to finish the growth of NPs. The obtained fresh NP solution was collected in the product collector (7). The NPs were precipitated using centrifuge at a speed of 12500 rpm for 10 min and the top supernatant was decanted. The precipitated NPs were dissolved into the same volume of NMP. The centrifuge process was repeated twice and the final black slurry in the bottle was dried under vacuum and kept in the desiccators for future use. Part of the sample was stored in the air or re-dispersed into deionized (DI) water for the long-term stability evaluation.

Synthesis of $(CoFe)_{(1-x)}Al_x@Al_{(1-y)}(CoFe)_yO\text{-}(OH)_z$ NPs. Briefly, PVP of 0.2193 g (Mw = 10000), $CoCl_2{\cdot}6H_2O$ of 0.074 g (0.311 mmol), $FeCl_2{\cdot}4H_2O$ of 0.072 g (0.362 mmol) and $AlCl_3$ of 0.059 g (0.554 mmol) were dissolved into 50 mL NMP to form the metal-salt solution. $NaBH_4$ of 0.2 g (5.26 mmol) was dissolved into 50 mL NMP to form the reducing solution. Then, the microfluidic synthesis was performed at 85°C under inert atmosphere (nitrogen) protection using the following procedure: 20 mL of metal-salt solution and 20 mL of reducing solution were sucked into each of the syringes and fixed in the platform of the syringe pump, which was introduced into the Y mixer (5) to finish the nucleation by the syringe pump at a flow rate of 0.8mL/min per pump, and then the solution entered into the microchannel (6) to finish the growth of NPs. The obtained fresh NP solution was collected in the product collector (7). The NPs were precipitated using centrifuge at a speed of 12500 rpm for 10 min and the top supernatant was decanted. The precipitated NPs were dissolved into the same volume of NMP. The centrifuge process was repeated twice and the final black slurry in the bottle was dried under vacuum and kept in the desiccators for future use. Part of the sample was stored in the air or re-dispersed into DI water for the long-term stability evaluation.

Synthesis of Fe_3O_4 NPs. The Fe_3O_4 NPs were synthesized according to our previously invented modified co-precipitation method.[58] The reactions were carried out in a 3-necked glass bottle under nitrogen bubbling that also plays a role of stirring the solution. The PVP-dispersed iron salt solution was prepared by mixing PVP (3.333 g, 1.10 mmol), $FeCl_3 \cdot 6H_2O$ (0.225 g, 0.83 mmol), and $FeCl_2 \cdot 4H_2O$ (0.114 g, 0.58 mmol) in DI water (100 mL). The mixture was heated to 60°C. NH_4OH solution (19 mL, 16 vol.%; concentration of original NH_4OH: 25%) was added dropwise using a constant pressure funnel for about 5 min and then the sodium citrate (TSC) solution (66.7 mL, 3.333 g, 11.33 mmol) was added dropwise for about 18 min. Subsequently maleic anhydride (MAH) solution (16.7 mL, 0.100 g, 1.03 mmol) was added dropwise at the same speed. After addition of the MAH solution, the mixture was heated to $95^{o}C$ and lasted for 2 hours and then stop heating to let the temperature drop to room temperature. The resulting black solution was centrifuged at 12500 rpm to permit the Fe_3O_4 NPs to settle out of the solution. The supernatant was decanted, and the same volume of DI water was added into the bottle, which was sonicated to form a uniform solution of NPs. The centrifuge process was repeated twice and the final black slurry in the bottle was dried under vacuum and kept in the desiccators for future use. Part of the sample was stored in the air or re-dispersed into DI water for the long-term stability evaluation.

Composition and structure characterization of nanohybrids. Morphologies, compositions and lattice fringes of nanohybrids were characterized by transmission electron microscopy (TEM; JOEL 2100F, 200kV) equipped with energy-dispersive X-ray spectroscopy (EDS). Powder X-ray diffraction (XRD) data of samples were collected on a D/max2200PC diffractometer (Cu Kα radiation, λ= 0.15418 nm, Rigaku, Japan). The X-ray photoelectron spectroscopy (XPS) was used to determine the elemental composition as well as chemical and electronic state of the related elements in NPs by detecting their thin films. XPS measurements were carried out on an ESCALAB 250 Thermo Electron Corporation with an Al Kα X-ray source (1486.6 eV). The core-level signals were obtained at a photoelectron take-off-angle of 45° (with respect to the sample surface). The X-ray source was run at a power of 300 W. The samples were mounted on the standard sample studs by means of double-sided adhesive tapes. The pressure in the analysis chamber was maintained at 2×10^{-9} mbar during each measurement. To compensate for surface charging effects, all binding energies (BE's) were referenced to the C 1s hydrocarbon peak at 284.6 eV.

Characterization of magnetic property. The magnetic properties were evaluated by room temperature hysteresis loop (RMHL) and/or thermo-magnetism (ZFC: zero-field cooling; FC: field cooling) curves measured by MPPS (SQUID) (Quantum design) using an applied magnetic field of 100Oe.

Characterization of magnetic resonance imaging (MRI) effects. MR scans for nanoparticle aqueous solution of different concentrations were carried out on a 3.0 tesla MR scanner (Signa Excite; GE Medical Systems, Milwaukee, WI), using an 8-channel head coil (GE Medical Systems). T_2-weighted spin-echo sequence with an echo time (TE) of 65 ms and pulse-repetition time (TR) of 3,000 ms and T_1-weighted spin-echo sequence with TE of 11 ms and TR of 300 ms were scanned. In order to measure longitudinal (T_1) and transverse (T_2) relaxation time of protons in aqueous nanoparticle solutions in a 3.0 T magnetic field, T_2-maping scanned by multi-echo spin-echo (SE) sequence and T_1-maping scanned by multi-flip angle 3-dimensional spoiled gradient-recalled acquisition (3D-SPGR) were obtained. Metal contents in the nanoparticle solutions for MRI measurements were determined by the inductively coupled plasma atomic emission spectroscopy (ICP-OES, Optima 7000 DV, PerkinElmer).

3. Results

Figure 1a is one wide-viewed TEM image of $Fe_{(1-x)}Zn_x@Zn_{(1-y)}Fe_yO\text{-}(OH)_z$ nanohybrids, suggesting that they are homogeneously dispersed with high uniformity. Histogram of their size distribution (Fig. s2a) gives a mean diameter of 3.2 ± 0.3 nm. Similar as other NPs less than 5 nm studied previously,[59] their XRD patterns only show broad and weak peaks (solid triangle: the (110) plane of bcc Fe, JCPDS No, 6-0696; void triangles: mixed multi-plane inflections from the metal oxides; Fig. 1c) even though the HRTEM image of typical single particles (Fig. 1b) reveals highly crystalline nature of these NPs. Although the wide-viewed TEM image of $Fe_{(1-x)}Zn_x@Zn_{(1-y)}Fe_yO\text{-}(OH)_z$ nanohybrids does not show clear core-shell morphology due to their small size, the HRTEM image (Fig. 1b) suggests the core–shell structure according to their Z-contrast and crystal lattice differences between the inner part and the surface coating. The crystal lattices in the core and the shell of the $Fe_{(1-x)}Zn_x@Zn_{(1-y)}Fe_yO\text{-}(OH)_z$ particle can be indexed as the Zn doping bcc Fe (110) planes (0.203 nm), the (102) plane of Fe-doped ZnO (0.193 nm) and the (101) plane of $ZnFe_2O_4$ (0.246 nm) by referring to their formation mechanism and XRD characterization.

The electronic structure of the consisting elements in the NPs can be well-defined by X-ray photoelectronic spectroscopy (XPS), giving further composition information of these NPs. The depth of the photo-emitted electrons escaping from the very top surface of samples excitated by the Al K_α X-ray source (1486.6 eV photons) is usually in the 0.5 - 3 nm range, comparable to the top surface or half of the diameter of these NPs. Thereby, XPS not only reveals the electronic structures of elements in cores and surfaces whether they are metallic or oxidized, but also provides additional evidence for their core-shell morphologies. The full XPS spectrum for $Fe_{(1-x)}Zn_x@Zn_{(1-y)}Fe_yO\text{-}(OH)_z$ NPs is plotted in Figure s2b, confirming the existence of Fe, Zn, O, C, B and N in these NPs. Carbon can be mainly from the stabilizer, or PVP. Boron can be from the decomposition of some $NaBH_4$ and the reducing reaction. The resulted metallic boron can be used as alloy element in metallic cores while B_2O_3 can dope in the oxide coatings.[23] The nitrogen can be attributed to the stabilizer (i.e., PVP) and/or the formation of metal-nitrogen bonds as the formed organometallic intermediates decompose.[29]

The high-resolution XPS spectrum for Zn of $Fe_{(1-x)}Zn_x@Zn_{(1-y)}Fe_yO\text{-}(OH)_z$ nanohybrids (Fig. 1d) shows two asymmetric peaks centered at 1023.3 eV and 1046.3 eV, which can be indexed as Zn 2p3/2 and Zn 2p1/2, respectively. The peaks at 711.9 eV and 725.3 eV in the high resolution XPS of Fe (Fig. 1e) represent Fe 2p3/2 and Fe 2p1/2. $ZnFe_2O_4$ should exist in $Fe_{(1-x)}Zn_x@Zn_{(1-y)}Fe_yO$-$(OH)_z$ NPs according to the distinct shake up peak at 719.7 eV and the XRD analysis (Fig. 1c). The asymmetry feature (low energy tails of the peaks) in Figure 1d and the weak peak at 706.6 eV in Figure 1e suggest existence of metallic Zn and Fe, which can be mainly attributed to the ultra-small FeZn alloy cores. In addition, existence of hydroxide zinc and iron cannot be ruled out according to their XPS characterization. Accordingly to the above XRD, HRTEM and XPS analysis, it can be reasonably deduced that the Fe-Zn NPs should be made of Zn-alloyed bcc Fe ($Fe_{(1-x)}Zn_x$, x<1) as cores, and Fe-doped wurtzite ZnO and $Zn(OH)_2$ and/or $ZnFe_2O_4$ as shells ($Zn_{(1-y)}Fe_yO$-$(OH)_z$, y<1).

It is well known that CoFe NPs have superior magnetic proeprties among various magnetic nanoparticles. Encouraged by the synthesis of $Fe_{(1-x)}Zn_x@Zn_{(1-y)}Fe_yO$-$(OH)_z$ NPs, this strategy was further extended to the synthesis of $(CoFe)_{(1-x)}Al_x@Al_{(1-y)}(CoFe)_yO$-$(OH)_z$ NPs using Co and Fe salts as the primary salts and $AlCl_3$ as the secondary salt. Figure 2a is the wide-viewed TEM image of $(CoFe)_{(1-x)}Al_x@Al_{(1-y)}(CoFe)_yO$-$(OH)_z$ nanohybrids, suggesting that they are homogeneously dispersed with high uniform and discernable core-shell morphologies. Histograms of their core and shell size distributions (Fig. s3a, s3b) suggest that these NPs have a core diameter of 2.4 ± 0.3 nm and a shell thickness of 1.2 ± 0.1 nm. Their powder X-ray diffraction (XRD) patterns (Fig. 2b) only show several broad peaks due to the small size effect.[59] Peaks at 23.7^o, $32.9\ ^o$, 35.4^o, 38.6^o, 54.5^o, 57.0^o and 75.1^o can be indexed as the (012), (104), (110), (113), (024), (116) and (119) planes of α-Al_2O_3 (JCPDS No.: 46-1212), doped by Co and Fe atoms or ions. Peaks at 44.7^o and 62.9^o can be indexed as the (110) and (200) planes of body-centered cubic (bcc) CoFe phase (JCPDS No.: 10-71-7173) possibly alloyed by Al. In order to observe their core–shell structures more clearly, high-resolution TEM (HRTEM) images of some single nanoparticles were characterized. Figure 2c and 2d are two angle-tilted HRTEM images for one single particle with the diameter of about 5.4 nm that clearly reveal different crystal lattices in the center and the edge of particles, which represents the (110) plane of bcc CoFe (0.202 nm) and the (110) plane of α-Al_2O_3 (0.238 nm), respectively, by recalling their XRD pattern (Fig. 2b).

Similar as $Fe_{(1-x)}Zn_x@Zn_{(1-y)}Fe_yO\text{-}(OH)_z$ NPs, the full XPS spectrum of $(CoFe)_{(1-x)}Al_x@Al_{(1-y)}(CoFe)_yO\text{-}(OH)_z$ NPs (Fig. s3c) not only confirms the existence of Co, Fe, Al and O, but also of C, B and N in the NPs. The high resolution XPS spectrum for Al element (Fig. 2e) shows one broad assymetric peak. Shoulders at 73.4 eV, 72.9 eV and 72.7 eV can be referred to the signals from Al 2p1/2, Al 2p and the binding energy (BE) of metallic Al 2p3/2, respectively. The full XPS spectrum also reveals the BE of metallic Al, which can be from metallic Al alloyed CoFe cores. Several shoulders at 75.8 eV and 74.3~74.8 eV can be indexed as Al 2p BEs from AlO_x or $Al(OH)_3$, respectively, which can be doped by Co and Fe in shells. Interestingly, there is a distinct shoulder at 73.9 eV that can be possibly indexed as Al 2p BE of Al-N bonds formed by the decomposition of Al-based intermediates. The shoulder at 73.9 eV clearly suggests the existence of Al-N bonds in these nanohybrids, indicating the formation of strong binding between NPs and PVP/NMP. The high energy resolution XPS spectrum for Fe element (Fig. 2f) shows pronounced peaks at 710.2~711.5 eV and 724.5 eV, indexed as Fe 2p3/2 and Fe 2p1/2, which suggests that iron oxides are mainly of Fe_3O_4 and FeO mixed with Al_2O_3 in shells by checking the peak position of O1s (531.1 eV, Fig s3c). A shoulder at 706.6 eV can be observed from the asymmetric feature of the peak at 710.2~711.5 eV, which can be attributed to the 2p3 BE of metallic Fe. Two distinct peaks at 781.4 eV and 797.2 eV in the high resolution XPS of Co (Fig. 2g) can be referred as Co 2p3/2 and Co 2p1/2, respectively, which can be from the Co and Fe doped AlO_x. Shoulders at 780.5 eV and 779.3 eV reveal the existence of $Co(OH)_2$ and CoO. The distinct shake-up peaks at 803.5 ev and 787.5 eV suggest the existence of $Al_2(CoFe)O_4$. The shoulder at 778.2 eV and the weak peak at 793.4 eV suggest the existence of metallic Co, which can be mainly attributed from CoFeAl alloy cores. Combination of the Fe 3s BE at 91.0 eV and Co 3s BE at 101.8 eV from the full XPS spectrum (Fig. s3c) of these NPs, the penetration depth of XPS (0.5-3.0 nm) and the shell thickness (~1.2 nm), Al alloying bcc phase CoFe as cores ($(CoFe)_{(1-x)}Al_x$, $x<1$) and hydroxide-group functionalized Co/Fe-doping Al_2O_3 as shells ($Al_{(1-y)}(CoFe)_yO$-$(OH)_z$, $y<1$) can be reasonably revealed by recalling their HRTEM and XRD characterization.

In order to further confirm their core shell structure, the metal ratios of the whole particles measured by EDX (Figure s4) and of the top surface parts measured by XPS were summarized in Table 1. Comparing with the theoretical values calculated by the metal content used in feeds, Zn matches Fe more than Al matches CoFe. Clearly, the experimental Fe/Zn ratio (74/26) in the whole $Fe_{(1-x)}Zn_x@Zn_{(1-y)}Fe_yO$-$(OH)_z$ nanohybrids is almost the same as the designed value (72/28) while the Al content (14%) in the real $(CoFe)_{(1-x)}Al_x@Al_{(1-y)}(CoFe)_yO$-$(OH)_z$ particles is far less than the designed value (46 atom%). The Al content (78 atom %) in the top surface of $(CoFe)_{(1-x)}Al_x@Al_{(1-y)}(CoFe)_yO$-$(OH)_z$ nanohybrids is much higher than that in the whole particles, indicating that these nanohybrids are indeed made of CoFe-rich cores (i.e., Al doping CoFe) and Al-rich shells (CoFe doping AlO-$(OH)_z$) by recalling their HRTEM, XRD and XPS analysis. The Zn content (77 atom%) in the top part of $Fe_{(1-x)}Zn_x@Zn_{(1-y)}Fe_yO$-$(OH)_z$ nanohybrids is also much higher than that in the whole particles, indicating that these nanohybrids are indeed made of Fe rich cores (i.e., Zn doping bcc Fe) and Zn rich shells (Fe doping ZnO) by recalling their HRTEM, XRD and XPS analysis.

These gradient core-shell nanohybrids preserve unique magnetic properties that were examined by SQUID. Their room temperature hysteresis loops (RTHLs) and thermal-magnetism measurements (zero-field cooling (ZFC) and field-cooling (FC) curves with an applied field of 100 Oe) are plotted in Figure 3, whose magnetic parameters are summarized in Table 2. Their RTHLs (Fig. 3a-b) suggest mono-phase nominal ferromagnetic feature at room temperature. Clearly, $(CoFe)_{(1-x)}Al_x@Al_{(1-y)}(CoFe)_yO$-$(OH)_z$ NPs have higher magnetism sensitivity and saturation than $Fe_{(1-x)}Zn_x@Zn_{(1-y)}Fe_yO$-$(OH)_z$ NPs. Their ZFC and FC curves (Fig. 3c) clearly confirm that they are superparamagnetic at room temperature. The non-zero coercivity and large bias of $Fe_{(1-x)}Zn_x@Zn_{(1-y)}Fe_yO\text{-}(OH)_z$ NPs (Table 3) are clearly attributed to enhanced magnetic surface anisotropy due to the strong pining effect from asymmetric coated Fe doped ZnO layers (Fig. 1b) since the magnetic dipole interaction among particles in compact-powder samples during measurements can reduce their coercivities (H_cs) and the magnetic anisotropy can increase the magnetic reverse barrier (or increase coercivity).[4,23,54,57] Clearly, the coating of $Al_{(1-y)}(CoFe)_yO\text{-}(OH)_z$ shells on $(CoFe)_{(1-x)}Al_x$ cores does not increase the magnetic anisotropy of $(CoFe)_{(1-x)}Al_x@Al_{(1-y)}(CoFe)_yO\text{-}(OH)_z$ NPs as much as that of $Fe_{(1-x)}Zn_x@Zn_{(1-y)}Fe_yO\text{-}(OH)_z$ NPs due to their small cores and uniform thick shells, leading to the almost zero bias and coercivity. In $(CoFe)_{(1-x)}Al_x@Al_{(1-y)}(CoFe)_yO\text{-}(OH)_z$ nanohybrids, the increased magnetic anisotropy can be balanced by the increased interfacial magnetic coupling, leading to almost zero bias and reduced coercivity, by comparing with those in CoFe NPs. However, there is a discernable vertical magnetism shift in $Fe_{(1-x)}Zn_x@Zn_{(1-y)}Fe_yO\text{-}(OH)_z$ NPs by comparing with that in pure Fe NPs[56], suggesting that the interfacial energy is increased more than the effective Zeeman energy in these NPs by coating the assymetric Fe doped ZnO shells. These results also indicate that surface anisotropies and pinning effects, affected by compositions, shell thickness and uniformity, dominate the coercivities and thermal-magnetism much more in NPs with small sizes than in large NPs.[4,14,30,43,54]

Generally, these nanohybrids preserve unique superparamagnetic properties due to their alloying effects, the proximity effects among components and the steric effects (completeness and thickness of coatings, core sizes). Comparing their magnetic properties with the Fe or CoFe NPs[57], these hybrid NPs with uniform $Al_{(1-y)}(CoFe)_yO\text{-}(OH)_z$ shells or assymetric $Zn_{(1-y)}FeO\text{-}(OH)_z$ coatings preserve more distinct superparamagnetic festures with reduced coercivities, reduced merging temperature (T_m), disappearance of ZFC peaks or much-matched freezing temperature (T_f) and T_m.

Molecular imaging is one trend of medical imaging in the future due to their fast, noninvasive, high 3-dimensional spatial resolution and soft tissue sensitive advantage.[58,60-62] Magnetic resonance imaging (MRI) is much adept at morphological imaging and functional imaging.[25,58] To achieve molecular imaging of disease biomarkers, mode-integrated MRI contrast agents with high specificity, high relaxation and biocompatibility are required.[25,48,58,61] Therefore, magnetic resonance imaging effects of these two kinds of nanohybrids were evaluated.

Figure 4 gives the effective-metal (Fe, or Co and Fe) concentration dependent T_1-weighted spin echo imaging (T_1WI) and T_2-weighted spin echo imaging (T_2WI) effects effects and the corresponding T_1 and T_2 relaxation rates of $Fe_{(1-x)}Zn_x@Zn_{(1-y)}Fe_yO\text{-}(OH)_z$ NPs (Fig. 4a: T_1^{-1}; Fig. 4b: T_2^{-1}) and $(CoFe)_{(1-x)}Al_x@Al_{(1-y)}(CoFe)_yO\text{-}(OH)_z$ (Fig. 4c: T_1^{-1}; Fig. 4d: T_2^{-1}). The MR images are remarkable with very high signal intensity in T_1-weighted image (brighter, top images in Fig. 4a and 4b) and low signal intensity in T_2-weighted image (darker, top images in Fig. 4b and 4d). Their T_1 relaxations show a rapid linear increase with the increase of concentration (Fig. 4a, 4c), giving the T_1 relaxation rates (slopes) of 0.046 $(\mu g\text{-}Fe/ml)^{-1}\cdot s^{-1}$ for $Fe_{(1-x)}Zn_x@Zn_{(1-y)}Fe_yO\text{-}(OH)_z$ NPs and 0.156 $(\mu g\text{-}CoFe/ml)^{-1}\cdot s^{-1}$ for $(CoFe)_{(1-x)}Al_x@Al_{(1-y)}(CoFe)_yO\text{-}(OH)_z$, respectively. Their T_2 relaxations also show a rapid linear increase trend with the increase of concentration (Fig. 4b, 4d) at dosages no more than 25 µg-metal/mL, giving the T_2 relaxation rates (slopes) of 0.311 $(\mu g\text{-}Fe/ml)^{-1}\cdot s^{-1}$ for $Fe_{(1-x)}Zn_x@Zn_{(1-y)}Fe_yO\text{-}(OH)_z$ NPs and 0.486 $(\mu g\text{-}CoFe/ml)^{-1}\cdot s^{-1}$ for $(CoFe)_{(1-x)}Al_x@Al_{(1-y)}(CoFe)_yO\text{-}(OH)_z$, respectively.

4. Discussion

Results of their application performances as MRI contrast agents indicate that these nanohybrids show good T_1WI and T_2WI imaging effects. Their linear T_1 and T_2 relaxation rates (Fig. 4) on the effective metal concentrations in the investigated concentration range are similar to previous results for various contrast agents,[25,48,63] which can be clearly explained by the following equation.[64]

$$T_{i,C}^{-1} = T_{i,0}^{-1} + R_i C \qquad (5)$$

Where, $T_{i,C}$ and $T_{i,0}$ (I = 1 or 2) represent the relaxation times of samples at C concentrations and zero concentration of contrast reagents and Ri denotes the relaxation rate of magnetic nanoparticles, and C represents the concentration of nanoparticles homogeneously distributed in the aqueous solution.

Most commonly spin echo (SE) MRI pulse sequence is used for T_1- and T_2-weighted spin echo imaging and the signal intensity for SE pulse sequence is defined as:[65]

$$I = I_0(1 - e^{-T_R/T_1}) \times e^{-T_E/T_2} \qquad (6)$$

Intensity (I) of T_1 weighted spin echo image (T_1WI) is purely T_1-dependent while T_2 weighted spin echo image (T_2WI) is purely T_2 dependent; T_1- and T_2-weighting can be achieved by eliminating the T_2 term (T_2 term → 1) for T_1 weighting and T_1 term (T_1term → 1) for T_2 weighting with the selection of the appropriate combination of T_E (time of echo) and T_R (time of repetition) value.

In the evaluation of T_1WI imaging effects, T_E and T_R are set as 11 ms and 300 ms. Clearly, the T_2 term (e^{-T_E/T_2}) in equation 6 can be almost 1 due to the much short T_E as T_2 is enough long, leading to the signal intensity increase in T_1 weighted spin echo image (brighter, the top images of Fig. 4a and 4c) with the increase of the incorporated nanoparticle concentration (T_1 becomes shorter by equation 5). While in the evaluation of T_2WI imaging effects, T_E anf T_R are set as 65 ms and 3000 ms. Correspondingly, the T_1 term ($1 - e^{-T_R/T_1}$) in equation 6 can be almost 1 due to the much long T_R as T_1 is enough short, leading to the signal intensity decrease in T_2 weighted spin echo image (darker, the top images of Fig. 4b and 4d) with the increase of the nanoparticle concentration (T_2 becomes shorter by equation 5).

Figure 4 suggests that $(CoFe)_{(1-x)}Al_x@Al_{(1-y)}(CoFe)_yO\text{-}(OH)_z$ NPs preserve higher T_1 and T_2 relaxation rates than $Fe_{(1-x)}Zn_x@Zn_{(1-y)}Fe_yO\text{-}(OH)_z$ NPs. The enhanced T_1 and T_2 relaxation rates (T_1^{-1} and T_2^{-1}) of superparamagnetic NPs depend upon the involved relaxation mechanism that relys on their microstructure, surface and magnetic properties. [48] High magnetism sensitivity and saturation can increase the frequency of molecule moving near to that of the proton spins around the nanohybrids, or an accelerated spin-lattice relaxation (short T_1). Recalling to their magnetic properties, $(CoFe)_{(1-x)}Al_x@Al_{(1-y)}(CoFe)_yO\text{-}(OH)_z$ NPs have higher magnetism sensitivity and saturation, leading to enhanced T_1 relaxation. The surface/interface features in $Fe_{(1-x)}Zn_x@Zn_{(1-y)}Fe_yO\text{-}(OH)_z$ NPs and their high coercivity can increase the spin-spin relaxation time (or large T_2), showing reduced T_2WI imaging effects. Therefore, $(CoFe)_{(1-x)}Al_x@Al_{(1-y)}(CoFe)_yO\text{-}(OH)_z$ NPs preserve better T_1WI and T_1WI effects than $Fe_{(1-x)}Zn_x@Zn_{(1-y)}Fe_yO\text{-}(OH)_z$ NPs at the investigated concentration range.

In order to further evaluate their efficiency as MRI contrast agents, the T_1WI and T_2WI effects of one commercial positive MRI contrast agent (e.g., gadopentetate dimeglumine, Gddm) for route clinics and the recently-developed superparamagnetic iron oxide (SPIO) NPs (self-made) were evaluated at the same condition for comparison. The morphology and size distribution of the synthesized SPIO NPs are shown in Figure s5, revealing the highly crystalline magnetite spinel Fe_3O_4 nanoparticles with a mean diameter of 7.1 ± 1.2 nm. Figure 5a and 5b give the T_1WI and T_2WI effects of Gddm, respectively. Figure 5c and 5d show the T_1WI and T_2WI effects of SPIO, respectively. The derived R_1 and R_2 relaxation rates of T_1WI and T_2WI and the R_2/R_1 ratios of these nanohybrids were calculated and summarized in Table 3, comparing with the synthesized nanohybrids.

The concentration dependent image intensities and T_1 and T_2 relaxation show the similar results as $(CoFe)_{(1-x)}Al_x@Al_{(1-y)}(CoFe)_yO\text{-}(OH)_z$ and $Fe_{(1-x)}Zn_x@Zn_{(1-y)}Fe_yO\text{-}(OH)_z$ NPs. Clearly, $(CoFe)_{(1-x)}Al_x@Al_{(1-y)}(CoFe)_yO\text{-}(OH)_z$ NPs, $Fe_{(1-x)}Zn_x@Zn_{(1-y)}Fe_yO\text{-}(OH)_z$ NPs and SPIO show better T_1WI and T_2WI effects (high R) than Gddm. A remarkable result is that $(CoFe)_{(1-x)}Al_x@Al_{(1-y)}(CoFe)_yO\text{-}(OH)_z$ NPs exhibit higher R_1 and lower R_2/R_1 than those of SPIO, indicating that $(CoFe)_{(1-x)}Al_x@Al_{(1-y)}(CoFe)_yO\text{-}(OH)_z$ NPs can play as a better positive contrast agent than SPIO. SPIO has the highest R_2/R_1 and R_2 values, suggesting that SPIO is still the best negative contrast agent among these contrast agents. By comparing

R_2/R_1 ratios of $Fe_{(1-x)}Zn_x@Zn_{(1-y)}Fe_yO\text{-}(OH)_z$ NPs and $(CoFe)_{(1-x)}Al_x@Al_{(1-y)}(CoFe)_yO\text{-}(OH)_z$, the former can be a better negative contrast than the later.

Since eyes of people are more sensitive to bright signal, the T_1WI is preferred in the disease diagnosis. The mostly used contrast agents for the T_1WI are made of gadolinium compounds (e.g., gadopentetate dimeglumine), which is used at a comparable concentration of about 335 μg-metal/mL, much higher than these nanohybrids. This high dosage definitely increases the risk of the release of potential toxic gadolinium into body. Here, the developed nanohybrids for MRI contrast agents, particularly $(CoFe)_{(1-x)}Al_x@Al_{(1-y)}(CoFe)_yO\text{-}(OH)_z$ NPs, have much more excellent T_1WI effect ($R_1 = 0.156\ (\mu g/mL)^{-1}\cdot s^{-1}$) than the commercial Gd-based positive contrast (e.g., Gddm: $R_1 = 0.022\ (\mu g/mL)^{-1}\cdot s^{-1}$). Overdose of these nanohybrids can be efficiently avoided for the future clinical applications due to their low dosages for enough high signals. Therefore, these newly developed nanohybrids are highly desired as MRI contrast agents.

Conclusions

The developed core alloying and gradient shell doping strategy shows great potentials in structure and composition controlled design and surface/interface modification of magnetic nanoparticles. Nanohybrids made of metal alloy as cores and doped metal oxide as shells, such as $(CoFe)_{(1-x)}Al_x@Al_{(1-y)}(CoFe)_yO\text{-}(OH)_z$ and $Fe_{(1-x)}Zn_x@Zn_{(1-y)}Fe_yO\text{-}(OH)_z$ nanohybrids, have been successfully synthesized according to this strategy using the programmed microfluidic and batch cooling process. These nanohybrids exhibit unique magnetic properties due to the interface magnetic coupling and magnetic anisotropy significantly affected by the core alloying and the gradient doping of metal oxide shells, and surface chemical properties (i.e., rich of M-OH, $MO\text{-}(OH)_z$ and /or M-N bonds). The combined effects from their unique magnetic properties and surface properties endow them dual-mode MRI effects with high-sensitivity by comparing with the Gd-based contrast agent. Particularly, $(CoFe)_{(1-x)}Al_x@Al_{(1-y)}(CoFe)_yO\text{-}(OH)_z$ exhibit much better T_1WI performance (high R_1) than the commercial Gd based positive contrast agents (e.g., gadopentetate dimeglumine) and SPIO, which shall be an excellent positive MRI contrast agent. As for SPIO, it is still an excellent negative MRI contrast agent (high R_2 and R_2/R_1 ratio).

Acknowledgements This work was supported by NSFC (Grant No. 51371018 and 50971010), the Fundamental Research Funds for the Central Universities (FRF-BR-14-001B).

References

1 Chen, G. *et al.* Interfacial Effects in Iron-Nickel Hydroxide–Platinum Nanoparticles Enhance Catalytic Oxidation. *Science* **344**, 495-499 (2014).

2 Zhang, Z., Xu, B. & Wang, X. Engineering Nanointerfaces for Nanocatalysis. *Chem Soc Rev* **43**, 7870-7886, doi:DOI: 10.1039/C3CS60389J (2014).

3 Jiang , R., Li , B., Fang, C. & Wang, J. Metal/Semiconductor Hybrid Nanostructures for PlasmonEnhanced Applications *Adv. Mater.* **26**, 5274–5309 (2014).

4 Song, Y., Ding, J. & Wang, Y. Shell Dependent Evolution of Optical and Magnetic Properties of Co@Au Core-shell Nanoparticles. *J Phys Chem C* **116**, 11343-11350 (2012).

5 Belotelov, V. I. *et al.* Plasmon-mediated magneto-optical transparency. *Nature Communication* **4**, 2128 (2013).

6 Vasiliev, R. B., Babynina, A. V. & Maslova, O. A. Photoconductivity of nanocrystalline SnO_2 sensitized with colloidal CdSe quantum dots *J. Mater. Chem. C* **1**, 1005-1010 (2013).

7 Song, Y. *et al.* Magneto-Plasmons in Periodic Nanopore Structures. *Scientific Reports* **4**, 4991 (2014).

8 Song, Y., Wang, Y., Li, B. B., Fernandes, C. & Ruda, H. E. Interfacial Interaction Induced Self-Assembly of Nanoparticles into Superstructures. *Nanoscale* **5**, 6779 - 6789, doi:DOI: 10.1039/c3nr01366a (2013).

9 Li, S. *et al.* Controlled Hybridization of Sn-SnO2 Nanoparticles via Simple Programmed Microfluidic Processes for Tunable Ultraviolet and Blue Emissions. *J. Mater. Chem. C* **2**, 7687-7694, doi:10.1039/c4tc00842a (2014).

10 Duan, S. & Wang, R. Au/$Ni_{12}P_5$core/shell nanocrystals from bimetallic heterostructures:in situ synthesis, evolution and supercapacitor properties. *NPG Asia Materials* **6**, e00 (2014).

11 Chen, L., Xie, C. & Chen, Y. Optimization of the Power Conversion Efficiency of Room Temperature-Fabricated Polymer Solar Cells Utilizing Solution Processed Tungsten Oxide and Conjugated Polyelectrolyte as Electrode Interlayer *Adv. Funct. Mater.* **24**, 3986-3995 (2014).

12 Ong, Q. K., Lin, X.-M. & Wei, A. Role of Frozen Spins in the Exchange Anisotropy of Core-Shell Fe@Fe_3O_4 Nanoparticles. *J. Phys. Chem. C* **115**, 2665-2672 (2011).

13 Zhou, B., Tao, L., Tsang, Y. H. & Jin, W. Core-shell nanoarchitecture: a strategy to significantly enhance white-light upconversion of lanthanide-doped nanoparticle. *J. Mater. Chem. C* **1**, 4313-4318 (2013).

14 Sellmyer, D. J. *et al.* Novel structures and physics of nanomagnets (invited). *J. Appl. Phys.* **117**, 172609 (2015).

15 Malyutin, A. G. *et al.* Viruslike Nanoparticles with Maghemite Cores Allow for Enhanced MRI Contrast Agents. *Chem. Mater.* **27**, 327-335 (2015).

16 Huang, J. *et al.* Crystal engineering and SERS properties of Ag–Fe3O4 nanohybrids: from heterodimer to core–shell nanostructures. *J. Mater. Chem.* **21**, 17930-17937 (2011).

17 Belotelov, V. I. *et al.* Enhanced magneto-optical effects in magnetoplasmonic crystals. *Nature Nanotech.* **6**, 370-376 (2011).

18 Montero, M. I. *et al.* Nanostructures and the proximity effect. *J. Phys. D: Appl. Phys.* **35**, 2398-2402 (2002).

19 Song, Y. *et al.* Magnetic and electric property evolution of amorphous cobalt-rich alloys driven by field annealing. *J. Phys. D: Appl. Phys.* **45** 225001 (2012).

20 Song , Y., Wang, Y. H., JI, S. & Ding, J. Shell-Driven Fine Structure Transition in Co@Au Core-shell Nanoparticles. *Nano-Micro Lett.* **4**, 235-242 (2012).

21 Song, Y., Sun, P., Henry, L. L. & Sun, B. Mechanism for Structure and Performance Controlled Preparation of Thin Film Composite Membrane via Interfacial Polymerization. *J. Membr. Sci.* **251**, 67-72 (2005).

22 Wang, L. *et al.* Hierarchical SnO_2 Nanospheres: Bio-inspired Mineralization, Vulcanization, Oxidation Techniques, and the Application for NO Sensors. *Scientific Reports* **3**, 3500 (2013).

23 Song, Y. *et al.* In-situ Redox Microfluidic Synthesis of Core-Shell Nanoparticles and their Long-term Stability. *J. Phys. Chem. C* **117**, 17274-17284 (2013).

24 Banthí, J. C. *et al.* High Magneto-Optical Activity and Low Optical Losses in Metal-Dielectric Au/Co/Au–SiO2 Magnetoplasmonic Nanodisks. *Adv. Mater.* **24**, OP36-OP41 (2012).

25 Jin, Y., Jia, C., Huang, S.-w., O'Donnell, M. & Gao, X. Multifunctional nanoparticles as coupled contrast agents. *Nature Communication* **1**, 41 (2010).

26 Chen, G. *et al.* Interfacial Effects in Iron-Nickel Hydroxide–Platinum Nanoparticles Enhance Catalytic Oxidation *Science* **344** 495-499 (2014).

27 Wu, Q. *et al.* Tuning magnetic anisotropies of Fe films on Si(111) substrate via direction variation of heating current. *Scientific Reports* **3**, 1547 (2013).

28 Chin, J. Y. *et al.* Nonreciprocal plasmonics enables giant enhancement of thin-film Faraday rotation. *Nature Communication* **4**, 1599 (2013).

29 Wang, R. *et al.* A General Strategy for Nanohybrids Synthesis via Coupled Competitive Reactions Controlled in a Hybrid Process. *Sci. Rep.* **5**, 9189 (2015).

30 Berkowitz, A. E., Sinha, S. K., Fullerton, E. E. & Smith, D. J. Exchange bias mediated by interfacial nanoparticles (invited). *J. Appl. Phys.* **117**, 172607 (2015).

31 Tang, Z., Song , Y., Sun, S., Zhang, T. & Jiang, Y. Magnetic Field Driving Gradient Effects on the Microstructure in Amorphous-nanocrystalline Cobalt Alloy Ribbons. *Nanoscale* **4**, 386-393, doi:DOI: 10.1039/c1nr10968e (2012).

32 Wen, T. & Krishnan, K. M. Thermal Stability and Morphological Transformations of Au_{core}-Co_{shell} Nanocrucibles. *J Phys Chem C* **114**, 14838-14842 (2010).

33 Wang, D., Zhao, P. & Li, Y. General preparation for Pt-based alloy nanoporous nanoparticles as potential nanocatalysts. *Scientific Reports* **1**, 37 (2011).

34 Li, S. *et al.* Controlled hybridization of Sn-SnO2 nanoparticles via simple-programmed microfluidic processes for tunable ultraviolet and blue emissions. *Journal of Materials Chemistry C* **2**, 7687-7694, doi:10.1039/C4TC00842A (2014).

35 Ruan, Z. *et al.* Controllable preparation of nanocomposites through convenient structural modification of cobalt contained organometallic precursors: nanotubes and nanospheres with high selectivity, and their magnetic properties. *J. Mater. Chem. C* **2**, 633-640 (2014).

36 Kim, M. & Song, H. Precise adjustment of structural anisotropy and crystallinity on metal-Fe_3O_4hybrid nanoparticles and its influence on magnetic and catalytic properties. *J. Mater. Chem. C* **2**, 4997-5004 (2014).

37 Vural, M., Crowgey, B., Kempel, L. C. & Kofinas, P. Nanostructuredflexible magneto-dielectrics for radio frequency applications. *J. Mater. Chem. C* **2**, 756-763 (2014).

38 Herman, D. A. J. *et al.* Hot-injection synthesis of iron/iron oxide core/shell nanoparticles for T2 contrast enhancement in magnetic resonance imaging. *Chem. Comm.* **47**, 9221-9223 (2011).

39 Farmer, J. A. & Campbell, C. T. Ceria Maintains Smaller Metal Catalyst Particles by Strong Metal-Support Bonding. *Science* **329**, 933-935 (2010).

40 Song, Y., Kumar, C. S. S. R. & Hormes, J. Microfluidic Synthesis of Nanomaterials. *Small* **4**, 698-711 (2008).

41 Marre, S. & Jensen, K. F. Synthesis of micro and nanostructures in microfluidic systems *Chem. Soc. Rev.* **39**, 1183-1202 (2010).

42 Nightingale, A. M. *et al.* Large-scale synthesis of nanocrystals in a multichannel droplet reactor. *J. Mater. Chem. A* **1**, 4067-4076 (2013).

43 Song, Y. & Henry, L. L. Nearly Monodispersion CoSm Nanoparticles Synthesized by a Microfluidic reactor. *Nanoscale Res. Lett.* **4**, 1130-1134 (2009).

44 Chen, Y., Ma, J., Li, Q. & Wang, T. Gram-scale synthesis of ultrasmall SnO_2 nanocrystals with an excellent electrochemical performance. *Nanoscale* **5**, 3262–3265 (2013).

45 Biswas, S., Miller, J. T., Li, Y., Nandakumar, K. & Kumar, C. S. S. R. Developing a Millifluidic Platform for the Synthesis of Ultrasmall Nanoclusters: Ultrasmall Copper Nanoclusters as a Case Study. *Small* **8**, 688-698 (2012).

46 Sebastian, V., Arruebo, M. & Santamaria, J. Reaction Engineering Strategies for the Production of Inorganic Nanomaterials *Small* **10**, 835-853 (2014).

47 Li, Y. *et al.* A facile fabrication of large-scale reduced graphene oxide–silver nanoparticle hybrid film as a highly active surface-enhanced Raman scattering substrate. *J. Mater. Chem. C* **3**, doi:10.1039/c5tc00196j (2015).

48 Gupta, H., Paul, P., Kumar, N., Baxi, S. & Das, D. P. One pot synthesis of water-

dispersible dehydroascorbic acid coated Fe_3O_4 nanoparticles under atmospheric air: Blood cell compatibility and enhanced magnetic resonance imaging. *Journal of Colloid and Interface Science* **430**, 221-228 (2014).

49 Zhang, J., Tang, Y., Lee, K. & Ouyang, M. Nonepitaxial growth of hybrid core-shell nanostructures with large lattice mismatches. *Science* **327**, 1634-1638 (2010).

50 Poppe, J., Gabriel, S., Liebscher, L., Hickey, S. G. & Eychmuller, A. A versatile approach for coating oxidic surfaces with a range of nanoparticulate materials. *J. Mater. Chem. C* **1**, 1515-1524 (2013).

51 Erdem, E. Y., Cheng, J. C., Doyle, F. M. & Pisano, A. P. Multi-Temperature Zone, Droplet-based Microreactor for Increased Temperature Control in Nanoparticle Synthesis. *Small* **10**, 1076-1080 (2014).

52 Edel, J. B., Fortt, R., deMello, J. C. & deMello, A. J. Microfluidic routes to the controlled production of nanoparticles. *Chem. Comm.* **1136-1137** (2002).

53 Khan, S. A. & Duraiswamy, S. Controlling bubbles using bubbles-microfluidic synthesis of ultra-small gold nanocrystals with gas-evolving reducing agents. *Lab Chip* **12**, 1807-1812 (2012).

54 Song, Y., Henry, L. L. & Yang, W. T. Stable Cobalt Amorphous Nanoparticles Formed by an In-situ Rapid Cooling Microfluidic Process *Langmuir* **25** 10209-10217 (2009).

55 Park, J. I., Saffari, A., Kumar, S., Gunther, A. & Kumacheva, E. Microfluidic synthesis of polymer and inorganic particulate materials. *Annu. Rev. Mater. Res.* **40**, 415-443 (2010).

56 Shen, X. *et al.* Spatiotemporal-resolved nanoparticle synthesis via simple programmed microfluidic processes. *RSC Advances* **4**, 34179-34188, doi:10.1039/C4RA04168B (2014).

57 Shen, X. *et al.* Spatiotemporal-Resolved Ultra-small Nanoparticle Synthesis via Simple Programmed Microfluidic Processes. *RSC Advances* **4**, 34179-34188, doi:10.1039/c4ra04168b (2014).

58 Song, Y. *et al.* Synthesis of Well-dispersed Aqueous-phase Magnetite Nanoparticles and their Metabolism as MRI Contrast Agent for Reticuloendothelial System *European Journal of Inorganic Chemistry*, 3303-3313 (2011).

59 Song, Y. *et al.* Microfluidic synthesis of cobalt nanoparticles. *Chem. Mater.* **18**, 2817-2827 (2006).

60 Tang, W. *et al.* Fe_5C_2 Nanoparticles with High MRI Contrast Enhancement for Tumor Imaging *Small* **10**, 1245-1249 (2014).

61 Walter, A. l. *et al.* Mastering the Shape and Composition of Dendronized Iron Oxide Nanoparticles To Tailor Magnetic Resonance Imaging and Hyperthermia. *Chem. Mater.* **26**, 5252-5264 (2014).

62 Zhou, Z. *et al.* Anisotropic Shaped Iron Oxide Nanostructures: Controlled Synthesis and Proton Relaxation Shortening Effects. *Chem. Mater.* **27**, 3505-3515 (2015).

63 Seo, W. S. *et al.* FeCo/graphitic-shell nanocrystals as advanced magnetic-resonance-imaging and near-infrared agents. *Nature Materials* **5**, 971-976 (2006).

64 Okuhata, Y. Delivery of diagnostic agents for magnetic resonance imaging. *Advanced Drug Delivery Reviews* **37**, 121-137 (1999).

65 Schröder, L. & Faber, C. *Basic contrast mechanisms: in In Vivo NMR Imaging Methods and Protocols*. 45-67 (Humana Press, Springer, 2011).

Table 1 Metal element ratio in feeds, in the whole particles measured by EDX and in the surface parts of nanohybrids measured by XPS

Sample	Designed atomic ratio	Experimental atomic ratio	Top surface atomic ratio by XPS
$(CoFe)_{(1-x)}Al_x@Al_{(1-y)}(CoFe)_yO\text{-}(OH)_z$	Co/Fe/Al: 25/29/46	Co/Fe/Al: 46/40/14	Co/Fe/Al: 10/12/78
$Fe_{(1-x)}Zn_x@Zn_{(1-y)}Fe_yO\text{-}(OH)_z$	Fe/Zn: 72/28	Fe/Zn: 74/26	Fe/Zn: 23/77

Table 2 Magnetic properties of nanohybrids

Sample	Size, nm	^aH_c, Oe		^bM_o, emu/g		^cT_f K	^dT_m K
		left	right	$M_{0,t}$	$M_{0,b}$		
$(CoFe)_{(1-x)}Al_x@Al_{(1-y)}(CoFe)_yO\text{-}(OH)_z$	Core: 2.42 ± 0.30; Shell: 1.20 ± 0.12	-0.9	0.8	0.07	0.05	106	106
$Fe_{(1-x)}Zn_x@Zn_{(1-y)}Fe_yO\text{-}(OH)_z$	3.22 ± 0.26	-18	27	0.34	-0.52	<2	<2
^{e}CoFe	2.74 ± 0.20	-16	17	0.13	-0.13	71	125
^{e}Fe	3.52 ± 0.28	-37	37	0.63	-0.62	141	348

^{a} Hc: coercivity; ^{b} $M_{0,t}$, and $M_{0,b}$: magnetism at zero field in the top and bottom cycle of HL;^{c} T_f: the freezing temperature above which the NPs gradually shift from clusters-glass (CG) like state to the ferromagnetic (FM) state; ^{d} Tm: the merging temperature for zero-field-cooling curves (M_{ZFC}(T)) and field-cooling curves (M_{FC}(T)), indicating that the NPs are in the same FM state for ZFC and FC processes above that temperature; ^{e} Data from reference: Shen X., et al., RSC Adv. 4(2014)34179.[56]

Sample	R_1 (μg/mL)$^{-1}$·s^{-1}	R_2 (μg/mL)$^{-1}$·s^{-1}	R_2/R_1
$Fe_{(1-x)}Zn_x@Zn_{(1-y)}Fe_yO\text{-}(OH)_z$	0.046	0.311	6.76
$(CoFe)_{(1-x)}Al_x@Al_{(1-y)}(CoFe)_yO\text{-}(OH)_z$	0.156	0.486	3.11
Gadopentetate dimeglumine	0.022	0.025	1.14
SPIO	0.121	5.066	41.9

Table 3 T_1 and T_2 relaxation rates R_1, R_2, R_2/R_1 ratios for $Fe_{(1-x)}Zn_x@Zn_{(1-y)}Fe_yO\text{-}(OH)_z$, $(CoFe)_{(1-x)}Al_x@Al_{(1-y)}(CoFe)_yO\text{-}(OH)_z$ NPs, gadopentetate dimeglumine and SPIO

Figure Captions

Figure 1 TEM image (a), HRTEM image (b), XRD (c), high energy resolution XPS for Zn (d) and high energy resolution XPS for Fe (e) of $Fe_{(1-x)}Zn_x@Zn_{(1-y)}Fe_yO\text{-}(OH)_z$ nanohybrids. JCPDS No for XRD analysis: bcc Fe, 6-0696; wurtzite ZnO, 89-1397. ▼: the corresponding metallic phases; ∇: the corresponding metal oxides.

Figure 2 TEM image (a), XRD (b), angle tilt HRTEM images (c, d), high energy resolution XPS for Al (e), high energy resolution XPS for Fe (f) and high energy resolution XPS for Co (g) of $(CoFe)_{(1-x)}Al_x@Al_{(1-x)}(CoFe)_xO\text{-}(OH)_z$ nanohybrids. JCPDS No for XRD analysis: bcc CoFe, 10-71-7173; $\alpha\text{-}Al_2O_3$, 46-1212. ▼: the corresponding metallic phases; *: the corresponding metal oxides.

Figure 3 The full range (a) and the central part (b) of room temperature hysteresis loop and the thermo-magnetism curves (c) (ZFC: zero-field cooling; FC: field cooling) of $(CoFe)_{(1-x)}Al_x@Al_{(1-x)}(CoFe)_xO\text{-}(OH)_z$ (black curves) and $Fe_{(1-x)}Zn_x@Zn_{(1-y)}Fe_yO\text{-}(OH)_z$ (red curves) nanohybrids.

Figure 4 Magnetic-resonance imaging (MRI) effects of ultra-small $FeZn_x@Zn_{(1-y)}Fe_yO\text{-}(OH)_z$ and$(CoFe)_{(1-x)}Al_x@Al_{(1-x)}(CoFe)_xO\text{-}(OH)_z$ hybrid nanoparticle solutions. (a): the effective metal (Fe) concentration dependent T_1 relaxation rates and MR images (top images) of $Fe_{(1-x)}Zn_x@Zn_{(1-y)}Fe_yO\text{-}(OH)_z$ nanoparticles generated on a T_1-weighted spin-echo sequence with T_E of 11 ms and T_R of 300 ms. (b): the effective metal concentration dependent T_2 relaxation rates and MR images (top images) of $Fe_{(1-x)}Zn_x@Zn_{(1-y)}Fe_yO\text{-}(OH)_z$ nanoparticles generated on a T_2-weighted spin-echo sequence with an echo time (T_E) of 65 ms and pulse-repetition time (T_R) of 3000 ms. (c) the effective metal (Co and Fe) concentration dependent T_1 relaxation rates and MR images (top images) of $(CoFe)_{(1-x)}Al_x@Al_{(1-x)}(CoFe)_xO\text{-}(OH)_z$ nanoparticles generated on a T_1-weighted spin-echo sequence with T_E of 11 ms and T_R of 300 ms. (d): the effective metal (Co and Fe) concentration dependent T_2 relaxation rates and MR images (top images) of $(CoFe)_{(1-x)}Al_x@Al_{(1-x)}(CoFe)_xO\text{-}(OH)_z$ nanoparticles on a T_2-weighted spin-echo sequence with an echo time (T_E) of 65 ms and pulse-repetition time (T_R) of 3000 ms. Metal concentrations in solutions are determined by ICP-AES and EDS. Concentration unit: μg-metal/mL in the top images.

Figure 5 Magnetic-resonance imaging (MRI) effects of gadopentetate dimeglumine (M_w =938.1, Beijing BeiLu Pharmaceutical Co.,Ltd.) and superparamagnetic iron oxide (SPIO) nanoparticle solutions. (a): the effective metal (Gd) concentration dependent T_1 relaxation rates and MR images (top images) of gadopentetate dimeglumine solutions generated on a T_1-weighted spin-echo sequence with T_E of 11 ms and T_R of 300 ms. (b): the effective metal concentration dependent T_2 relaxation rates and MR images (top images) of gadopentetate dimeglumine solutions generated on a T_2-weighted spin-echo sequence with an echo time (T_E) of 65 ms and pulse-repetition time (T_R) of 3000 ms. (c) the effective metal (Fe) concentration dependent T_1 relaxation rates and MR images (top images) of SPIO nanoparticles generated on a T_1-weighted spin-echo sequence with T_E of 11 ms and T_R of 300 ms. (d): the effective metal (Fe) concentration dependent T_2 relaxation rates and MR images (top images) of SPIO nanoparticles generated on a T_2-weighted spin-echo sequence with an echo time (T_E) of 65 ms and pulse-repetition time (T_R) of 3000 ms. Concentration is based on Gd or Fe mass contents in solutions determined by ICP-AES. Concentration unit: µg-metal/mL in the top images.

Figure 1

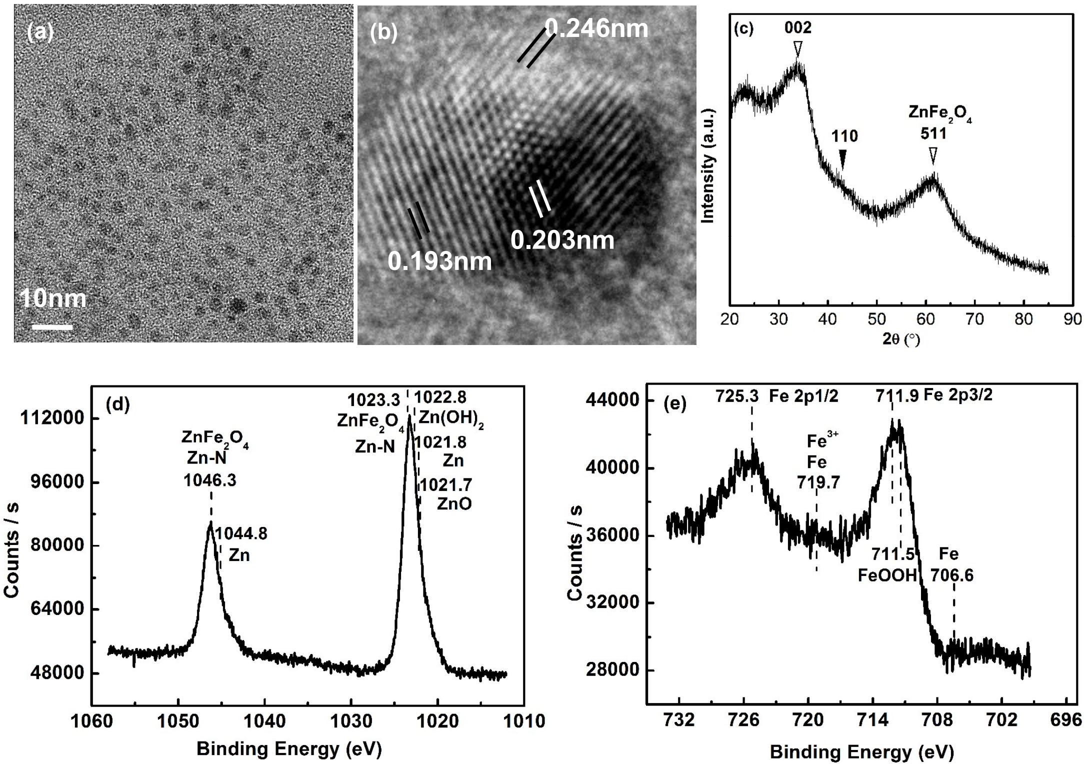
(a)
10nm
(b)
0.246nm
0.193nm
0.203nm
(c)
002
110
ZnFe$_2$O$_4$
511
Intensity (a.u.)
20
30
40
50
60
70
80
90
2θ (°)
(d)
ZnFe$_2$O$_4$
Zn-N
1046.3
1044.8
Zn
1023.3
ZnFe$_2$O$_4$
Zn-N
1022.8
Zn(OH)$_2$
1021.8
Zn
1021.7
ZnO
112000
96000
80000
64000
48000
Counts / s
1060
1050
1040
1030
1020
1010
Binding Energy (eV)
(e)
725.3 Fe 2p1/2
711.9 Fe 2p3/2
Fe^{3+}
Fe
719.7
711.5
FeOOH
Fe
706.6
44000
40000
36000
32000
28000
Counts / s
732
726
720
714
708
702
696
Binding Energy (eV)

Figure 2

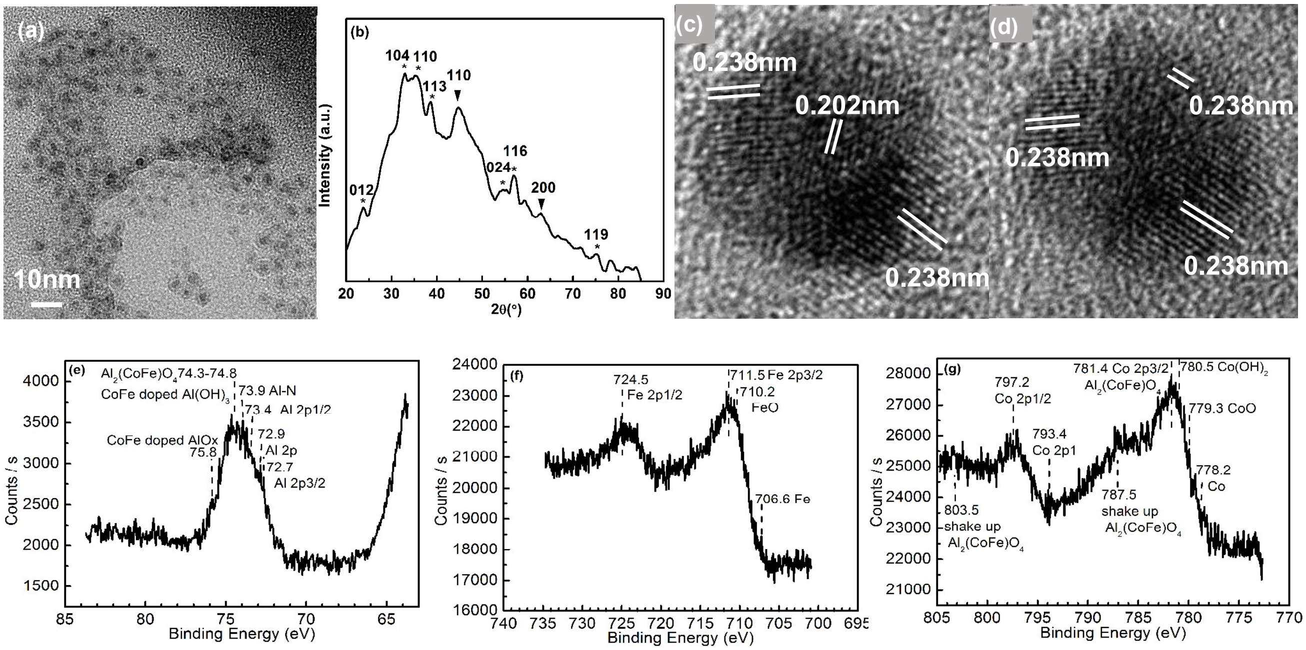
(a)
10nm
(b)
Intensity (a.u.)
2θ(°)
012
104
110
113
110
024
116
200
119
20 30 40 50 60 70 80 90
(c)
0.238nm
0.202nm
0.238nm
(d)
0.238nm
0.238nm
0.238nm
0.238nm
(e)
Al2(CoFe)O4 74.3-74.8
CoFe doped Al(OH)3
73.9 Al-N
73.4 Al 2p1/2
CoFe doped AlOx
75.8
72.9
Al 2p
72.7
Al 2p3/2
Counts / s
4000 3500 3000 2500 2000 1500
85 80 75 70 65
Binding Energy (eV)
(f)
724.5
Fe 2p1/2
711.5 Fe 2p3/2
710.2
FeO
706.6 Fe
Counts / s
24000 23000 22000 21000 20000 19000 18000 17000 16000
740 735 730 725 720 715 710 705 700 695
Binding Energy (eV)
(g)
797.2
Co 2p1/2
781.4 Co 2p3/2
Al2(CoFe)O4
780.5 Co(OH)2
779.3 CoO
793.4
Co 2p1
778.2
Co
803.5
shake up
Al2(CoFe)O4
787.5
shake up
Al2(CoFe)O4
Counts / s
28000 27000 26000 25000 24000 23000 22000 21000
805 800 795 790 785 780 775 770
Binding Energy (eV)

Figure 3

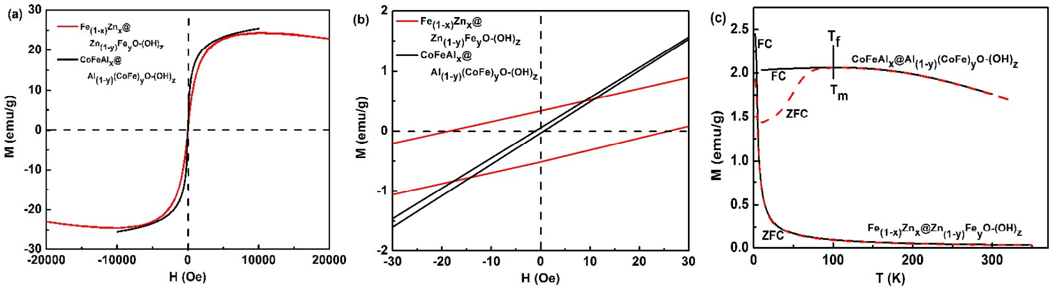
(a)
Fe(1-x)Znx@
Zn(1-y)FeyO-(OH)z
CoFeAlx@
Al(1-y)(CoFe)yO-(OH)z
M (emu/g)
30
20
10
0
-10
-20
-30
-20000
-10000
0
10000
20000
H (Oe)
(b)
Fe(1-x)Znx@
Zn(1-y)FeyO-(OH)z
CoFeAlx@
Al(1-y)(CoFe)yO-(OH)z
M (emu/g)
2
1
0
-1
-2
-30
-20
-10
0
10
20
30
H (Oe)
(c)
FC
Tf
CoFeAlx@Al(1-y)(CoFe)yO-(OH)z
FC
Tm
ZFC
Fe(1-x)Znx@Zn(1-y)FeyO-(OH)z
ZFC
M (emu/g)
2.5
2.0
1.5
1.0
0.5
0.0
0
100
200
300
T (K)

Figure 4

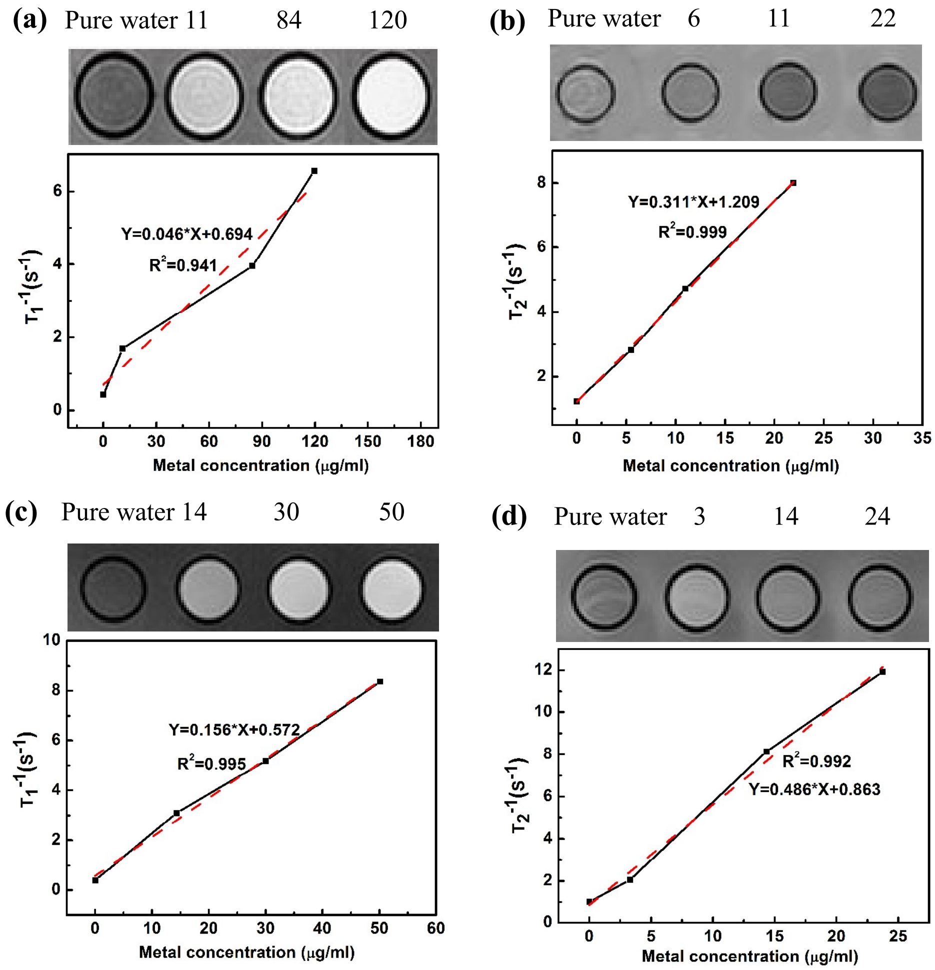
(a) Pure water 11 84 120
Y=0.046*X+0.694
R²=0.941
T1-1(s-1)
0 2 4 6
0 30 60 90 120 150 180
Metal concentration (μg/ml)
(b) Pure water 6 11 22
Y=0.311*X+1.209
R²=0.999
T2-1(s-1)
2 4 6 8
0 5 10 15 20 25 30 35
Metal concentration (μg/ml)
(c) Pure water 14 30 50
Y=0.156*X+0.572
R²=0.995
T1-1(s-1)
0 2 4 6 8 10
0 10 20 30 40 50 60
Metal concentration (μg/ml)
(d) Pure water 3 14 24
R²=0.992
Y=0.486*X+0.863
T2-1(s-1)
0 2 4 6 8 10 12
0 5 10 15 20 25
Metal concentration (μg/ml)

Figure 5

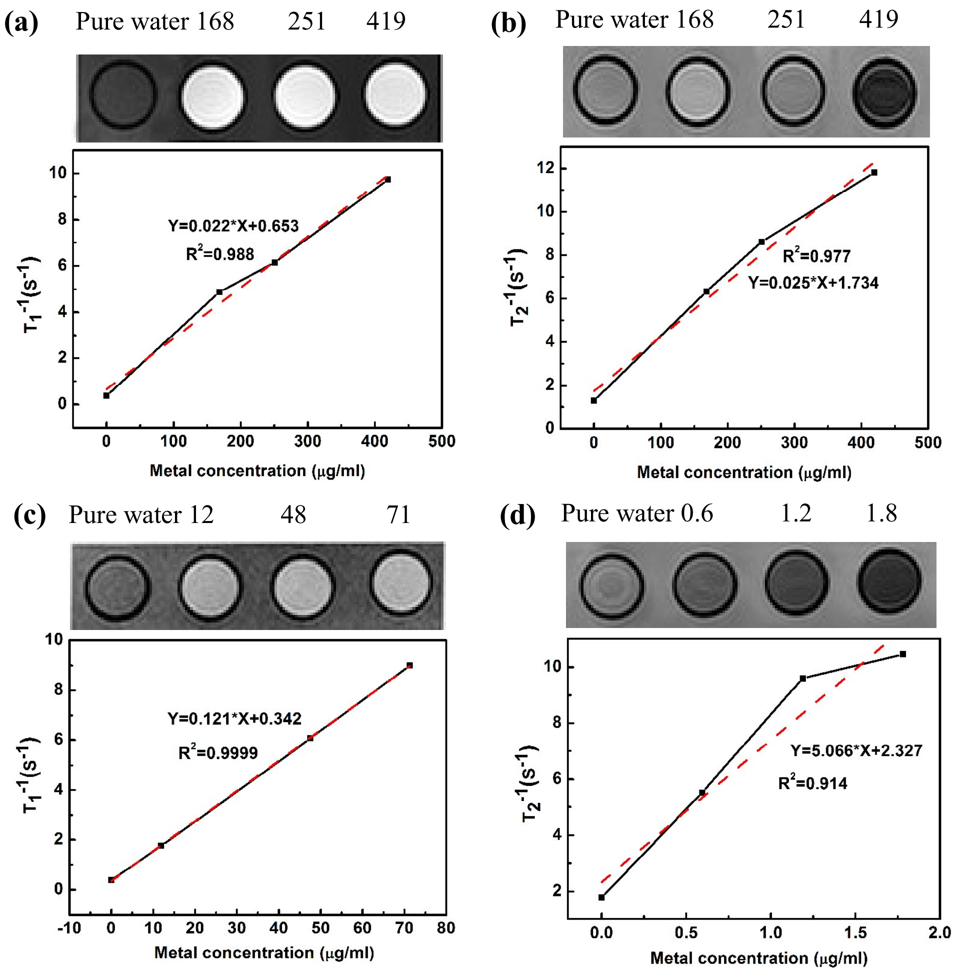
(a)
Pure water 168 251 419
Y=0.022*X+0.653
R^2=0.988
$T_1^{-1}(s^{-1})$
Metal concentration (μg/ml)
(b)
Pure water 168 251 419
R^2=0.977
Y=0.025*X+1.734
$T_2^{-1}(s^{-1})$
Metal concentration (μg/ml)
(c)
Pure water 12 48 71
Y=0.121*X+0.342
R^2=0.9999
$T_1^{-1}(s^{-1})$
Metal concentration (μg/ml)
(d)
Pure water 0.6 1.2 1.8
Y=5.066*X+2.327
R^2=0.914
$T_2^{-1}(s^{-1})$
Metal concentration (μg/ml)